Title

Bioresorbable silicon electronics for transient spatiotemporal mapping of electrical activity from the cerebral cortex.

Journal

Nature materials, 15(7)

ISSN

1476-1122

Authors

Yu, Ki Jun
Kuzum, Duygu
Hwang, Suk-Won
et al.

Publication Date

2016-07-01

DOI

10.1038/nmat4624

Peer reviewed

HHS Public Access

Author manuscript

Nat Mater. Author manuscript; available in PMC 2016 October 18.

Published in final edited form as:

Nat Mater. 2016 July ; 15(7): 782–791. doi:10.1038/nmat4624.

Bioresorbable Silicon Electronics for Transient Spatio-temporal Mapping of Electrical Activity from the Cerebral Cortex

Ki Jun Yu[#1,2], **Duygu Kuzum**[#3,4,5], **Suk-Won Hwang**[6], **Bong Hoon Kim**[2,7], **Halvor Juul**[8], **Nam Heon Kim**[2,7], **Sang Min Won**[1,2], **Ken Chiang**[9], **Michael Trumpis**[9], **Andrew G. Richardson**[4,10], **Huanyu Cheng**[11], **Hui Fang**[2,7], **Marissa Thomson**[3,4,12], **Hank Bink**[3,4], **Delia Talos**[8], **Kyung Jin Seo**[2,7], **Hee Nam Lee**[2,13], **Seung-Kyun Kang**[2,7], **Jae-Hwan Kim**[2,7], **Jung Yup Lee**[2,13], **Younggang Huang**[14], **Frances E. Jensen**[4,8], **Marc A. Dichter**[4,8], **Timothy H. Lucas**[4,10], **Jonathan Viventi**[9], **Brian Litt**[3,4,8,*], and **John A. Rogers**[1,2,7,*]

[1] Department of Electrical and Computer Engineering, University of Illinois at Urbana-Champaign, Urbana, IL 61801, USA

[2] Frederick Seitz Materials Research Laboratory, University of Illinois at Urbana-Champaign, Urbana, IL 61801, USA

[3] Department of Bioengineering, University of Pennsylvania, Philadelphia, Pennsylvania 19104, USA

[4] Center for Neuroengineering and Therapeutics, University of Pennsylvania, Philadelphia, PA 19104, USA

[5] Department of Electrical and Computer Engineering, University of California, San Diego, San Diego, CA 92093

[6] KU-KIST Graduate School of Converging Science and Technology, Korea University, Seoul 136-701, Republic of Korea

[7] Department of Materials Science and Engineering, University of Illinois at Urbana-Champaign, Urbana, IL 61801, USA

[8] Department of Neurology, Perelman School of Medicine, University of Pennsylvania, Philadelphia, PA 19104, USA

[9] Department of Biomedical Engineering, Duke University, Durham, NC 27708, USA

[10] Department of Neurosurgery, Perelman School of Medicine, University of Pennsylvania, Philadelphia, PA 19104, USA.

[*]To whom correspondence should be addressed. jrogers@illinois.edu or littb@upenn.edu.

Author contribution K.J.Y., D.K., B.L, and J.A.R designed the research; K.J.Y., D.K., S.W.H., B.H.K., N.H.K., S.M.W., K.C., K.J.S., H.N.L., S.K.K., J.H.K., and J.Y.L. fabricated the devices and electronics, K.J.Y., D.K., H.J., S.M.W., M.T., A.G.R., and J.V. conceived and performed experimental, and analysis, D.T. performed biocompatibility and histology studies, H.C., Y.H. performed mechanical simulations, and K.J.Y, D.K., A.G.R., M.T., J.V., B.L., and J.A.R. wrote the manuscript.

Author Information The authors declare there is no competing financial interests.

[11] Department of Engineering Science and Mechanics, Penn State University, University Park, PA 16802, USA.

[12] Department of Chemical and Biomolecular Engineering University of Pennsylvania, Philadelphia, Pennsylvania 19104, USA

[13] Department of Chemical and Biomolecular Engineering, University of Illinois at Urbana-Champaign, Urbana, IL 61801, USA

[14] Department of Mechanical Engineering and Department of Civil and Environmental Engineering, Northwestern University, Evanston, IL 60208, USA

[#] These authors contributed equally to this work.

Abstract

Bioresorbable silicon electronics technology offers unprecedented opportunities to deploy advanced implantable monitoring systems that eliminate risks, cost and discomfort associated with surgical extraction. Applications include post-operative monitoring and transient physiologic recording after percutaneous or minimally invasive placement of vascular, cardiac, orthopedic, neural or other devices. We present an embodiment of these materials in both passive and actively addressed arrays of bioresorbable silicon electrodes with multiplexing capabilities, that record in vivo electrophysiological signals from the cortical surface and the subgaleal space. The devices detect normal physiologic and epileptiform activity, both in acute and chronic recordings. Comparative studies show sensor performance comparable to standard clinical systems and reduced tissue reactivity relative to conventional clinical electrocorticography (ECoG) electrodes. This technology offers general applicability in neural interfaces, with additional potential utility in treatment of disorders where transient monitoring and modulation of physiologic function, implant integrity and tissue recovery or regeneration are required.

Neurophysiologic monitoring is commonly used for diagnosing and treating neurological disorders such as epilepsy, Parkinson's disease, depression, chronic pain and disorders of the peripheral nervous system[1,2]. Such capabilities are critically important for mapping and monitoring brain function during and in preparation for resective neurosurgery[3], such as for epilepsy and tumors, for assisting in neurodevice placement, such as for Parkinson's disease[4], epilepsy[5], and depression, and for guiding surgical procedures on complex, interconnected peripheral nerve structures such as the brachial, lumbar and sacral plexi[2]. Related functionality is also increasingly leveraged during intravascular procedures, such as aneurysm coiling[6], stent placement[7], AVM embolization[8], and endoscopic operations. Post-procedure monitoring typically occurs in an intensive care unit (ICU), where a variety of devices record physiologic activity, typically with limited temporal and spatial sampling, directly at the regions of interest, simply because these are exposed and accessible during surgery[9]. Intracranial monitors for postoperative seizures and recovery of brain function after surgery would also be useful, and potentially more sensitive than scalp monitoring[10]. These clinical needs motivate efforts to develop technologies for neurophysiologic monitoring that incorporate inorganic and organic nanomaterials in flexible formats[11-20]. Although it would be desirable for neuromonitoring in the ICU to offer the same high fidelity, high resolution performance as is available in the operating room, the morbidity and

cost of associated with additional surgeries to remove implanted recording devices preclude this possibility in general practice. In certain cases, such as in invasive intracranial electrocorticographic monitoring for epilepsy surgery, recording electrodes remain in place for one to three weeks to localize epileptic networks[21]. Here, removal occurs in a second procedure, often with resection of brain involved in generating seizures. In other cases, electrodes are placed in staging procedures that do not end in resection, but rather are done for broad lateralization in preparation for more extensive implants or placement of implantable devices. Here, a second procedure to remove implants adds cost and risk. Recent evidence suggests that 1-3 months of ambulatory intracranial recording may be required to adequately localize seizures for epilepsy surgery or device placement, a period prohibitively long for current in-hospital approaches[22]. Using bioresorbable electrodes for such studies would eliminate the danger and cost of removing standard electrodes at the end of this period, during which standard devices may become fibrosed or adherent to underlying tissues. An ideal scenario would involve placement of temporary, bioresorbable monitoring devices capable of providing continuous streams of data for guiding medical care over predetermined periods of time before dissolving. Below we present a new class of technology that offers this mode of operation, with spatio-temporal resolution that matches or exceeds any existing alternative.

Recently reported bioresorbable sensors of pressure and temperature in the intracranial space provide distinct, complementary capabilities in single-point measurements of non-electrical characteristics of the cerebrospinal fluid in the intracranial space[23]. The results presented here introduce materials and device designs for direct electrical interfaces to the brain itself, including bioresorbable electrodes and multiplexing electronics for high speed spatio-temporal mapping of biological processes. The platform builds on recently described technologies that exploit nanomembranes of device-grade, monocrystalline silicon (Si NMs) as the semiconductor foundation of a high performance class of electronic systems. The key enabling chemistry involves hydrolysis of Si NMs upon immersion in biofluids, to yield end products that are biocompatible. The results presented here indicate that Si NMs, at high levels of doping[24], can additionally serve as the neural recording electrodes themselves, as a stable, yet ultimately transient, measurement interface. In addition to their established bioresorbability, the nanoscale thicknesses of Si NMs, when deployed with thin substrates, interconnect metals and dielectrics, yield devices with levels of mechanical flexibility necessary for conformal contact and chronically stable interfaces with neural tissues. The following content describes means to exploit these concepts in materials, devices and system-level examples of bioresorbable Si electronic interfaces to the brain, with examples in passive and active matrix addressed recording *in vivo*. Evaluations include capture of ECoG and subdermal encephalograms (EEG) in live, awake animal models, where Si NMs serve as active materials both for the recording interface and for the backplane transistors that allow high speed multiplexed addressing across arrays of channels. Comprehensive *in vitro* and *in vivo* studies establish that these systems provide accurate and reproducible measurements of neural signals and physiological activity for acute (~hours) and chronic (up to 33 days) use. Biocompatibility studies reveal no overt tissue reactions compared to clinically approved commercial ECoG electrodes.

Figure 1a provides an exploded schematic diagram (left) of a magnified optical microscope image of the active sensing and the passivation regions (right) of a simplest embodiment of these concepts: a thin, flexible electrode array based on phosphorus doped (impurity concentrations: ~ 10^{20} /cm^3) collection of Si NM (thickness ~300 nm) structures. Here, a layer of SiO_2 (thickness ~100 nm) insulates the connection traces to isolate them from bio-fluids and adjacent tissue. The terminal pads consist of exposed Si, as the direct neural interface. A flexible sheet of the bioresorbable polymer poly(lactic-co-glycolic acid, PLGA, thickness ~30 μm) serves as the substrate. This array (3 × 4 mm^2) allows chronic recordings from rat cortex at four measurement sites, each with dimensions of 250 × 250 $μm^2$. Such small arrays serve effectively in demonstrator experiments and studies of the fundamental issues in the materials science. We note, however, that the materials and fabrication schemes align with those used in the semiconductor industry and are, as a result, immediately scalable to much larger areas, higher channel counts and smaller/larger electrode sizes. As an illustration, Figure 1b (bottom frames) presents a passive array that includes 256 independent channels, in a 16 × 16 configuration, with an overall area of 3 cm × 3.5 cm. Multiplexing architectures, described subsequently, provide routes to scaling to even higher numbers of channels. The fabrication steps appear in the methods section and in Supplementary Fig. 1. The lot and functional electrode yields are ~100% and >90%, respectively. Figures 1b (top) and Supplementary Fig. 2 show micrographs of completed arrays. Figure 1b (bottom) shows a scaled version of this same basic device architecture that includes 256 independent channels.

Placing an array onto a hydrogel substrate (Fig. 1c) and immersing the system in phosphate-buffered saline (PBS) at physiological pH (7.4) and at room temperature enables characterization of each of the electrodes by electrochemical impedance spectroscopy (EIS), across a range of frequencies most relevant to the studies described subsequently. In the recording of brain signals, the electrodes transduce ionic currents in the electrolyte to an electric current in the measurement system. The contact between an electrode and tissue has associated electrical impedance, where reductions in the impedance decrease the noise level, thereby increasing the signal to noise ratio (SNR) of the recordings[19,25]. The data in Fig. 1d correspond to the impedance (|Z|) of each channel in the array, along with the response of a gold (Au) electrode with the same dimensions. The EIS data for Si can be fit to an equivalent Randles circuit model (Supplementary Fig. 3a) that includes a double layer capacitance (C_{PE}) in parallel with a charge transfer resistance (R_{CT}), all of which is in series with a resistance (R_S) that corresponds to the surrounding electrolyte solution. This model quantitatively captures the EIS data for both Au (without the space charge layer) and Si electrodes, as shown in Supplementary Fig. 3b. The fitted values of C_{PE} are ~2.5 μF/cm^2 and ~10 μF/cm^2 for Si and Au, respectively; both values are in a range consistent with the literature[26,27]. The space charge layer lowers the capacitance of the Si electrode[28], causing the difference in capacitances for Au and Si electrodes (Fig. 1 d). More details of *in vitro* experiments of the Si electrodes are described in Supplementary Note 1 and Supplementary Figs 4-7.

The slow, controlled dissolution of Si NMs is critically important in their use as bioresorbable neural interfaces. Bioresorbable metals are less attractive options due to their comparatively fast dissolution kinetics, and tendency to crack, fragment and flake during the

process. Si dissolves under physiological conditions by hydrolysis to yield silicic acid, at rates that depend strongly on ionic content of the surrounding solution, pH, temperature and other factors, including the doping level. Specifically, Si forms neutral ortho-silicic acid $Si(OH)_4$ through an initial oxidation step to SiO_2 or through a direct equilibrium $Si+4H_2O \leftrightarrow Si(OH)_4+2H_2$[29,30]. Figure 1e illustrates the dissolution kinetics for highly boron and phosphorus doped (concentration of ~10^{20} /cm^3) Si NMs (~300 nm thick) in artificial cerebrospinal fluid (aCSF, pH 7.4) at physiological temperature (37 °C), evaluated by measuring the thicknesses at different time points by profilometry (Dektak, USA). Observations indicate that dissolution occurs in an exceptionally controlled, predictable process, without cracks, flakes, particulates or reduction in surface smoothness that often occurs in dissolution of metals. The dissolution rate exhibits a constant, thickness independent value of ~11 nm/day for these conditions. The dissolution characteristics of the other materials in the system, which for the case of the simple device in Fig. 1 are SiO_2 and PLGA, are also important, although less critical than the Si NMs due to their passive role in the device operation. Measurements indicate that SiO_2 and PLGA (75:25)[31] dissolve in biofluids at 37 °C at rates of ~8.2 nm/day (Supplementary Fig. 8), and complete dissolution time scales of ~4-5 weeks, respectively. Results of accelerated dissolution tests appear in Figure 1g as a series of images of a complete device collected at various times after immersion in PBS pH 10 at 37 °C. We estimate that the current device designs and material choices allow complete dissolution of the device in 2 months. Si and SiO_2 will dissolve within a month and 2 weeks, respectively, followed by PLGA. PLGA will dissolve in ~4-5 weeks. The materials parameters (i.e., thicknesses, doping levels for the Si, and ratio of lactide to glycolide for the PLGA) can be adjusted to achieve desired dissolution times.

For conformal contact against the curved surface of the brain, thin geometries and optimized mechanical layouts are important. Three dimensional finite element modeling (FEM) reveals distributions of principle strain for bending perpendicular to the interconnect direction, as in Fig. 1f (left). Based on the layouts and the mechanical moduli, the maximum strains in the SiO_2, Si and PLGA are less than 0.03 % for a bending radius of 1 mm, corresponding to the linear elastic regime for each of these materials. An optical image of a device wrapped around a glass rod with a radius of curvature of ~2 mm appears in Fig. 1f (right). Measurements before and after bending show negligible differences in impedance, consistent with expectation based both on FEM and analytical modeling results (Supplementary Fig. 9).

In vivo neural recording experiments involved the bioresorbable devices of Fig. 1 in adult rat animal models anesthetized and placed in a stereotaxic apparatus. A craniotomy exposed a 4×8 mm^2 region of cortex in left hemisphere (Fig. 2a), to allow positioning of a device on an area of the cortical surface next to a standard stainless steel microelectrode (7,850 μm^2) as a control for recording physiological oscillations under isofluorene anesthesia. Figure 2b shows representative sleep spindle activity captured by one of the channels in the bioresorbable array and the control electrode. Supplementary Fig. 10 show similar data for brain waves recorded during transition to deep anesthesia (Supplementary Fig. 10a) and K-complexes (Supplementary Fig. 10b) measured under anesthesia. Representative examples of pre-ictal and ictal-like spiking epileptiform activity induced by application of crystals of bicuculline methoxide recorded by the bioresorbable electrode and the control electrode

appear in Fig. 2c and d, respectively. The frequency of the pre-ictal spikes (Fig. 2c) increases and the inter-spike duration decreases as the time progresses, terminating into after discharges and ictal-like early epileptic discharges (Fig. 2d). The bioresorbable arrays can also be utilized as subdermal implants for high fidelity, recording of EEG and evoked potentials. Devices implanted on periosteum as described in Fig. 2e and Supplementary Fig. 11 yielded reliable recordings of theta waves (highlighted in power spectral analysis) and sleep spindles (Fig. 2f). Collectively, the results demonstrate that bioresorbable recording platforms can capture reliable physiological or pathological activity both intracortically and subdermally.

Chronic tests of ECoG recording indicate long-term stability in operation, where devices with increased thicknesses of SiO_2 (~300 nm) and Si NMs (~1000 nm) survive for more than one month. Such studies used a miniature interface board connected to the device via a flexible interconnect cable to a headstage (Supplementary Fig. 12) designed for use with rats. Details are explained in the Methods section. Figure 3 summarizes representative cortical potentials recorded by three electrodes in the bioresorbable array and by a nearby screw electrode as a control, captured on Days 1, 8, 15, 30, 32 (Supplementary Fig. 13), and 33 measured from the time of the surgical implantation. Figure 3a and Supplementary Figs 12 and 14 describe the surgical procedures and the post-surgical setups used in freely moving rats, respectively. ECoG potentials show physiological signals and brain oscillations with various temporal and spatial differences. High-amplitude seizure-like rhythmic spike discharges (Fig. 3g) appear occasionally, consistent with absence-like seizure activity observed in Long Evans Rats[32-34]. By all functional metrics (e.g. signal to noise ratio, ability to measure delta, theta, alpha, gamma, spindles and sometimes epileptic spikes), the devices operate in a stable fashion, largely without change in performance throughout the month of the study, until sudden failure, likely due to the development of an open circuit state in the vicinity of the interconnects. After day 33, signals from the bioresorbable device disappear; while those form the control persist, consistent with dissolution of at least some critical component of the device. For epilepsy patients the clinically relevant operational lifetime is several weeks. Here, bioresorbable devices could be embedded into particular clinical devices to monitor for early signs of failure during critical post-operative periods, such as measuring pressure and flow after intravascular aneurysm occlusion (coiling), placement of aortic or other vascular grafts, or procedures to seal cerebrospinal fluid (CSF) leaks. Currently monitoring is based upon clinical examination, or requires interventional radiology that is invasive, expensive and impractical for continuous monitoring over days to months.

Understanding the reactive tissue response is critical in assessing the potential for use in such clinical applications[35]. Tissue inflammation, encapsulation of the electrodes in fibrous tissue (glial scar) and neuronal death in the vicinity of the electrode are the most important issues related to clinical translation[36-38]. Studies of tissue reactions of bioresorbable electrode arrays involved chronic implants in 14 animals, with Pt electrodes cut into similar geometries from clinical subdural grids (Ad-Tech Medical Inc) as controls, as shown in supplementary Fig. 15. Figure 4 summarizes the results obtained according to procedures outlined in the methods section. Double label immunohistochemistry for GFAP and Iba-1 reveal glial cell activation at 4 weeks post-implant (Fig. 4). In both control and bioresorbable

devices, moderate subpial gliosis occurs at the implantation site, when compared to the control contralateral hemisphere. No significant astrogliosis is noted at distant sites within the ipsilateral hemisphere. Iba-1 immunohistochemistry demonstrates the presence of both resting ramified, as well as round activated microglia underneath the control electrode, which extends to the superficial layers I-III. In contrast, at the implantation site of the bioresorbable electrode, microglial cells show an almost exclusively ramified morphology. The contralateral side in both groups exhibits no microglial reaction. The sham-operated control demonstrates a similar moderate subpial gliosis, but with no change in microglial densities or morphology.

Actively multiplexed device designs enable high-resolution, high channel count neural interfaces by minimizing the number of wires needed for external data acquisition. In this context, Si NMs provide not only an excellent choice for the electrodes but also for the backplane electronics, including the necessary switching and buffer transistors as a scalable pathway toward systems with increased numbers of channels and area coverage. A fully bioresorbable design appears in Fig. 5a; a sequence of images at various stages of the fabrication appear on the right. This embodiment uses 128 n-channel metal-oxide-semiconductor field-effect transistors (MOSFETs), with Molybdenum (Mo) for the source, drain and gate electrodes, and SiO_2 (~100 nm) for the gate dielectrics. Additional layers of Mo and a trilayer of SiO_2 (~300 nm)/Si_3N_4 (~400 nm)/SiO_2 (~300 nm) form interconnects and interlayer dielectrics (ILD), respectively. A second layer of Mo (~300 nm) serves as column selects and additional sensing electrode pads. Another trilayer provides a blanket encapsulating layer that has openings only at the locations of the Mo interface electrodes. The amount of materials in a single device with active multiplexed addressing are 100 mcg of Mo, 1.43 mcg of Si, 306 mcg of SiO_2, 264 mcg of S_3iN_4, and 27 pg of P. For comparison, the daily intake limits, average daily intake values, and daily production of such materials appear in Supplementary Table 1. The chemistry, dissolution kinetics and biocompatibility of each of the constituent materials can be found elsewhere[39-46]. The lot and functional electrode yields are ~10-20% and ~80%, respectively. Failures arise from leakage currents associated with pinholes in the encapsulating layer, introduced by particulate contamination in our academic cleanroom facilities. Figure 5b presents photographs of a device, wrapped around a cylindrical tube, with an inset that shows arrays of active electrodes. Figure 5c summarizes the electrical properties of a representative n-type MOSFET, where the mobility and on/off ratio are ~400 $cm^2\ V^{-1}$ and ~10^8, respectively, as calculated using standard field-effect transistor models. Figure 5d shows *in vitro* measurements on a representative unit cell. The output response was consistent with the input signal, thereby indicating proper operation. Details of *in vitro* experiments are in Supplementary Note 2 and Supplementary Figs 16-20.

Figure 5e shows a sequence of images during accelerated dissolution in PBS pH 12 at 37 °C. PECVD Si_3N_4 and Mo[40, 41] dissolves in biofluids at pH 7.4 at 37 °C at a rate of ~5.1 nm/day (Supplementary Fig. 8) and ~16-25 nm/day, respectively. This system involves ~1.3 μm, ~800 nm, ~300 nm, ~600 nm and ~30 μm thick layers of PECVD SiO_2, Si_3N_4, Si, Mo and PLGA, respectively. PLGA, Si, and Mo in biofluids at 37 °C dissolve completely within in ~4-6 weeks. Both SiO_2 and Si_3N_4, dissolve in 6 months under the same conditions. Supplementary Fig. 20 shows results of measurements of gain across the array and

cumulative leakage current for a representative device immersed in PBS at pH 7.4. The average gain and yield were 94% and 100%, respectively.

Figure 6 provides details on *in vivo* recordings with a bioresorbable, multiplexed recording array. The leakage current is ~10 nA. The 64-electrode array was placed on the cortical surface of the left hemisphere of an anesthetized rat in a stereotaxic apparatus (Supplementary Fig. 21). Picrotoxin was applied topically to induce epileptiform activity, just prior to the placement of the array. The data reveal epileptic spikes and discharges that last ~1-3s (Supplementary Movie 1) and repeat every ~10-15s. A set of different epileptic spikes (clockwise spiral, lower right to upper left diagonal, upper left to lower right diagonal, and right to left sweep) is shown in Fig. 6a as representative recordings. The sequence of eight movie frames corresponding to each spike (Fig. 6b) clearly reveals the propagation of neural waves and associated spatial-temporally resolved patterns (Supplementary Movie 2-6). The delay maps represent the latency of the spike's peak at each site (Fig. 6c). Each spiking activity shows a distinctive spatial flow indicated by the yellow arrow in each delay map. RMS power maps, corresponding to each representative spike (Fig. 6c and Supplementary Fig. 22) show the spatially resolved patterns.

In addition to epileptiform activity, spatial distributions of low amplitude evoked cortical activity can be captured using the same device. Somatosensory evoked potential (SSEP) experiments were conducted in anesthetized rats using the bioresorbable multiplexed array on the surface of the exposed barrel cortex. Evoked potentials were produced by stimulating two different whiskers (B1 and E3, Fig. 6d), corresponding to the barrel cortex and estimated relative location (Fig. 6e). The temporally resolved patterns of the evoked potentials are shown in Fig. 6f. The spatial distribution of the amplitude of the evoked potentials measured at the cortical surface by the array is consistent with the relative location of the activated whiskers on the barrel cortex as described with the color map (Fig. 6g). These results collectively demonstrate an ability to record stimulus evoked and drug-induced neural activity with high SNR. The same materials and device architectures can be easily adapted to larger areas and increased channel counts with potential for use in large animal models and, in the future, for clinical monitoring applications.

The concepts introduced here form a robust foundation of capabilities in bioresorbable implantable electrode technology for various clinical problems, ranging from post-operation monitoring of brain activity to electrical monitoring of skeletal muscles or organ function. In all cases, the thin, flexible form factors minimize mechanical injury associated with implantation and chronic use. The use of Si as the active semiconductor material aligns the technology consumer electronics industry with the natural capacity to scale to higher densities of electrodes and larger areas.

METHODS

Fabrication of passive electrode arrays

Fabrication of the passive electrode arrays began with solid state phosphorus doping (PH-1000N Source, Saint Gobain, USA, 1000 °C for 10 minutes) of p-type device Si on a Si on insulator (SOI, top Si ~300 nm, SOITEC, France) wafer. Removing the buried oxide

layer of the SOI by wet etching with concentrated HF released the device Si as a Si NM, retrieved with a slab of the elastomer poly(dimethylsiloxane) (PDMS) and transfer-printed to a spin-cast bilayer of poly(methylmethacrylate) (PMMA, ~800 nm thick) and polyimide (PI, ~300 nm thick) on a Si wafer. Photolithography and reactive ion etching (RIE) defined a pattern of electrodes and interconnects in the Si NMs. Plasma enhanced chemical vapor deposition (PECVD) formed a layer of SiO_2 (thickness 100 nm) as encapsulation. Patterned etching with buffered oxide etchant removed the SiO_2 from the electrode regions. Spin casting and patterning a top coating of PI (~300 nm thick) placed the Si NM electrodes and interconnects near the neutral mechanical plane. Patterning a mesh structure across the multilayer (i.e. PI, SIO_2, PI and PMMA) by RIE followed by immersion in buffered oxide etchant exposed the base layer of PMMA to allow its dissolution in acetone. Retrieval onto a slab of PDMS enabled removal of the bottom exposed layer of PI by RIE. Transfer onto a film of PLGA (~30 μm thick), facilitated by heating to temperatures close to the glass transition of the PLGA (55~60 °C, lactide/glycolide ratio of 75:25 composition), followed by elimination of the top layer of PI by RIE completed the fabrication. Bonding an ACF cable to the terminal regions of the Si NM interconnects yielded connection points for interfaces to external data acquisition (DAQ) systems.

Fabrication of actively multiplexed electrode arrays

The fabrication began with growth of 200 nm of thermal oxide on a p-type SOI wafer (top Si ~320 nm, SOITEC), photolithography and immersion in buffered oxide etchant to create a mask for solid state phosphorus diffusion (1000 °C for 6 minutes) to define the source and drain contacts. Releasing, retrieving and transferring the doped Si NMs onto a temporary substrate, consisting of Si wafer with a bilayer coating of PI/PMMA, followed procedures similar to those described for passive electrode arrays. Photolithography and RIE etching patterned the Si NMs into geometries for an 8×8 array of unit cells, each consisting of two transistors connected in series for purpose of actively multiplexed readout. A thin layer of SiO_2 (PECVD at 220 °C, thickness ~100 nm) served as the gate dielectric. Buffered oxide etching through a photolithographically patterned mask formed openings through the SiO_2 to expose the source and drain contact regions. Photolithography and lift off in acetone defined a patterned layer of Mo (sputter deposited, thickness ~300 nm) for the gate electrodes and metal interconnects. Deposition of a trilayer of SiO_2 (~300 nm)/Si_3N_4 (~400 nm)/SiO_2 (~300nm) by PECVD formed the interlayer dielectric. Photolithography and buffered oxide etching created vertical interconnect access (via) holes for electrical connections between layers. An additional layer of Mo (thickness ~300 nm) patterned by photolithography and liftoff defined column select lines. Another trilayer of SiO_2 (~300 nm)/Si_3N_4 (~400 nm)/SiO_2 (~300nm) served as encapsulation, with openings at the locations of the sensing electrodes and peripheral contact pads for interfacing to an external DAQ system. A spin-cast layer of PI served as device passivation. Selective RIE and buffered oxide etching through these multilayer stacks (diluted PI/trilayers of inorganic materials/trilayers of inorganic materials/Diluted PI) formed mesh structures that enabled release of active layers from the temporary substrate by dissolving the PMMA layer in acetone. Transfer printing steps followed, according to procedures similar to those for the passive electrode fabrication.

In vivo acute recordings of epileptiform activity

The *in vivo* data Fig. 2 is representative of four different acute experiments, each of which lasted 5-6 hours. The procedures, which were approved by the Institutional Care and Use Committee of the University of Pennsylvania, involved an anaesthetized rat with its head fixed in a stereotaxic apparatus. Wild-type, adult Long Evans male and female rats were used. The animal was anesthetized with initially ketamine/xylazine and then isoflurane throughout the craniotomy and neural recordings. A craniotomy exposed a 4×8 mm region of cortex in either left or tight or in both hemispheres. All recordings were taken in reference to a distant stainless steel bone screw inserted through the skull during the surgery. A commercial stainless steel microwire electrode (~100 um stainless steel wire from California Fine Wire) placed at 0.5 mm depth from the cortical surface in close proximity to the bioresorbable electrodes served as a control during acute recordings. Neural data was acquired by a FHC multi-channel neural amplifier (FHC Inc, Bowdoin, ME, USA) and an acquisition system (16 bit Axon Instruments Digidata 1322A, Axon Instruments, Foster City, CA). Recordings were high pass filtered at 0.1 Hz. Neural recording data were analyzed offline using Clampfit software (Axon Instruments) and custom Matlab software for neural signal analysis.

In vivo acute recordings of evoked responses by whisker stimulation

The following procedures were approved by the Institutional Care and Use Committee of the University of Pennsylvania. One 150-g, Sprague-Dawley rat was anesthetized with a ketamine (60 mg/kg), dexdomitor (0.25 mg/kg) solution and placed in a stereotaxic frame. A craniotomy was performed to expose the right barrel cortex. A skull screw was placed in the left frontal bone to serve as the reference electrode for the recordings. The recording array was placed over the exposed cortical surface. A pair of needle stimulating electrode were inserted into the left mystacial pad at various locations. Brief electrical currents (~250-600 μA, 1 ms/phase, biphasic pulse) were passed between the electrodes to activate the intrinsic muscles of the vibrissae, causing a visible protraction of the whiskers. Current amplitude and electrode spacing was adjusted for focal activation, usually 1-4 whiskers. Cortical potentials evoked by the whisker stimulation were recorded at 781.25 samples/s.

In vivo chronic recordings

An adult Long Evans rat was anesthetized with isoflurane and placed in a stereotactic frame (David Kopf Instruments Tujunga, CA). Body temperature was maintained with a heating blanket and the eyes were covered with ointment to prevent drying. The skull was exposed and a large craniotomy (4×8 mm^2) was made between bregma and lambda and laterally to the midline. The electrode was placed on the exposed dura and a slurry of gel foam and saline was layered on top of the electrode. A screw electrode was placed contralaterally to the experimental array, with another such electrode placed posterior to lambda as a ground and reference. Additional screws were secured in the skull for anchoring. The skull and electrodes were then covered with dental cement and the connecting plug was secured on top. The rat was given meloxicam for postoperative pain and allowed to recover on a heating pad. The rat was given meloxicam daily for 3 days after surgery to minimize pain. After 1 week the animal was placed in a cage for video/EEG recording. EEG signals were collected

continuously from 3 channels on the array and from the screw. The signals were amplified and low pass filtered at 600 Hz (Multichannel Systems, Reutlingen, Germany) and sampled at 2000 Hz with a 16 bit digitizer (National Instruments, Austin, TX). Data was acquired using a custom written MATLAB routine.

Chronic evaluation of immunohistochemistry

Rats (n=14) were anesthetized and transcardiac perfusion was performed using phosphate buffered saline (PBS 10x, cat. # BM-220, Boston BioProducts, Ashland, MA), followed by 4% paraformaldehyde (PFA, cat. # BM-155, Boston BioProducts). Whole brains were then removed and post-fixed overnight at 4°C in the same 4% PFA solution. Subsequently, fixed brains were cryoprotected in 30% sucrose (cat. # 57-50-1, Sigma-Aldrich, Saint Louis, MO) at 4°C and coronal sections were cut at 20 μm using a Leica CM3050 S cryostat (Leica Biosystems Inc.). Serial sections, spanning the entire craniotomy site, were mounted on charged slides and stored at −20°C until use. For immunostaining, slides were first immersed in an antigen retrieval solution (0.1M citrate buffer, pH 6.0, cat# ab64214, Abcam, Cambridge, MA) and placed in a water bath at 95°C for 10 minute. After cooling, sections were rinsed in distilled water, incubated in a blocking solution containing 0.1% Triton X-100 (cat. # 9002-93-1, Sigma-Aldrich) and 5% normal goat serum (cat. # GS-0500, Equitech-Bio Inc., Kerrville, TX) for one hour at room temperature (RT) and then incubated overnight at 4 °C with the following primary antibodies: anti- Glial Fibrillary Acidic Protein (GFAP, 1:1000, cat. # SMI-22R, Covance, Princeton, NJ), and anti-ionized calcium binding adapter molecule 1 (Iba-1, 1:1000, cat. # 019-19741, Wako Chemicals USA, Inc., Richmond, VA). After 3×20-minute washes in PBS, sections were incubated with the corresponding fluorescent secondary antibodies (Alexa Fluor 488 goat anti-mouse IgG2b, 1:1000, cat. # A-21141, and Alexa Fluor 568 goat anti-rabbit IgG, 1:1000, cat. # A-11011, Invitrogen by Life Technologies, Grand Island, NY). After the final washes (3 × 20 min in PBS), the slides were cover-slipped with an anti-fade medium containing the nuclear stain DAPI (Fluoromount-G+DAPI, cat. # 0100-20, Southern Biotechnology, Birmingham, AL). Control sections were incubated with omission of one or both primary antibodies, adding only the secondary antibodies to exclude false-positive labeling. Slides were examined on an epifluorescence microscope (Zeiss Axioscope, Germany) and images were acquired with a 20× objective and a Spot RT3 digital camera, using the Spot Software 5.1 (Diagnostic Instruments, Sterling Heights, MI). Digital images were processed using Adobe Photoshop 12.0 (Adobe Systems, San Jose, CA).

Supplementary Material

Refer to Web version on PubMed Central for supplementary material.

Acknowledgements

K.J.Y. and co-workers are funded by the Defense Advanced Research Projects Agency. D.K. and B. L. acknowledges Penn Medicine Neuroscience Center Pilot Grant, T32- Brain Injury Research Training Grant (5T32NS043126-12), Mirowski Family Foundation, Neil and Barbara Smit. Figure 2e, 3a, and 6d images from 3D Rat Anatomy Software (www.biosphera.org)

References

1. Niedermeyer, E.; da Silva, FL. Electroencephalography: basic principles, clinical applications, and related fields. Lippincott Williams & Wilkins; 2005.
2. Stacey WC, Litt B. Technology insight: neuroengineering and epilepsy— designing devices for seizure control. Nat. Clin. Pract. Neurol. 2008; 4:190–201. [PubMed: 18301414]
3. McKhann GM, Schoenfeld-McNeill J, Born DE, Haglund MM, Ojemann GA. Intraoperative hippocampal electrocorticography to predict the extent of hippocampal resection in temporal lobe epilepsy surgery. Journal of neurosurgery. 2000; 93:44–52. [PubMed: 10883904]
4. Whitmer D, et al. High frequency deep brain stimulation attenuates subthalamic and cortical rhythms in Parkinson's disease. Frontiers in human neuroscience. 2012; 6
5. Litt B, et al. Epileptic seizures may begin hours in advance of clinical onset: a report of five patients. Neuron. 2001; 30:51–64. [PubMed: 11343644]
6. Shapiro M, Becske T, Sahlein D, Babb J, Nelson PK. Stent-supported aneurysm coiling: a literature survey of treatment and follow-up. American Journal of Neuroradiology. 2012; 33:159–163. [PubMed: 22033717]
7. Wholey MH, et al. Global experience in cervical carotid artery stent placement. Catheterization and Cardiovascular Interventions. 2000; 50:160–167. [PubMed: 10842380]
8. Frizzel RT, Fisher WS III. Cure, Morbidity, and Mortality Associated with Embolization of Brain Arteriovenous Malformations: A Review of 1246 Patients in 32 Series over a 35-Year Period. Neurosurgery. 1995; 37:1031–1040. [PubMed: 8584142]
9. McNett MM, Horowitz DA. International multidisciplinary consensus conference on multimodality monitoring: ICU processes of care. Neurocrit Care. 2014; 21:215–228.
10. Mayevsky A, Manor T, Meilin S, Doron A, Ouaknine GE. Real-time multiparametric monitoring of the injured human cerebral cortex–a new approach. Acta Neurochir. Suppl. 1998; 71:78–81. [PubMed: 9779150]
11. Khodagholy D, et al. In vivo recordings of brain activity using organic transistors. Nature Commun. 2013; 4:1575. [PubMed: 23481383]
12. Viventi J, et al. Flexible, foldable, actively multiplexed, high-density electrode array for mapping brain activity in vivo. Nature Neurosci. 2011; 14:1599–1605. [PubMed: 22081157]
13. Khodagholy D, et al. NeuroGrid: recording action potentials from the surface of the brain. Nature Neurosci. 2015; 18:310–315. [PubMed: 25531570]
14. Escabí MA, et al. A high-density, high-channel count, multiplexed μECoG array for auditory-cortex recordings. Journal of neurophysiology. 2014; 112:1566–1583. [PubMed: 24920021]
15. Qing Q, et al. Nanowire transistor arrays for mapping neural circuits in acute brain slices. Proc. Natl Acad. Sci. USA. 2010; 107:1882–1887. [PubMed: 20133836]
16. Xiang Z, et al. Ultra-thin flexible polyimide neural probe embedded in a dissolvable maltose-coated microneedle. J. Micromech. Microeng. 2014; 24:065015.
17. Tian B, et al. Three-dimensional, flexible nanoscale field-effect transistors as localized bioprobes. Science. 2010; 329:830–834. [PubMed: 20705858]
18. Kozai TDY, et al. Ultrasmall implantable composite microelectrodes with bioactive surfaces for chronic neural interfaces. Nat. Mater. 2012; 11:1065–1073. [PubMed: 23142839]
19. Kuzum D, et al. Transparent and flexible low noise graphene electrodes for simultaneous electrophysiology and neuroimaging. Nat. Commun. 2014; 5:5259. [PubMed: 25327632]
20. Vitale F, Summerson SR, Aazhang B, Kemere C, Pasquali M. Neural stimulation and recording with bidirectional, soft carbon nanotube fiber microelectrodes. ACS Nano. 2015; 9:4465–4474. [PubMed: 25803728]
21. Daube, J.; Rubin, D. Clinical Neurophysiology. Oxford University Press; New York, NY: 2009.
22. King-Stephens D, et al. Lateralization of mesial temporal lobe epilepsy with chronic ambulatory electrocorticography. Epilepsia. 2015; 56:959–967. [PubMed: 25988840]
23. Kang S-K, et al. Bioresorbable silicon electronic sensors for the brain. Nature. 2016; 530:71–76. [PubMed: 26779949]

24. Saha R, et al. Highly doped polycrystalline silicon microelectrodes reduce noise in neuronal recordings in vivo. IEEE Trans Neural Sys Rehab Eng. 2010; 18:489–97.
25. Fontes MBA. Electrodes for bio-application: recording and stimulation. J. Phys. Conf. Ser. 2013; 421:012019.
26. Oskam G, Long JG, Natarajan A, Searson PC. Electrochemical deposition of metals onto silicon. J. Phys. D: Appl. Phys. 1998; 31:1927–1949.
27. Zhang, XG. Electrochemistry of Silicon and its Oxide. Kluwer Academic; New York, NY: 2001.
28. Schmickler, W.; Santos, E. Interfacial Electrochemistry. Ch. 11. Springer; Berlin Heidelberg: 2010.
29. Morita M, Ohmi T, Hasegawa E, Kawakami M, Ohwada M. Growth of native oxide on a silicon surface. J. Appl. Phys. 1990; 68:1272.
30. Seidel H, Csepregi L, Heuberger A, Baumgartel H. Anisotropic etching of crystalline silicon in alkaline solutions: I. orientation dependence and behavior of passivation layers. J. Electrochem. Soc. 1990; 137:3612.
31. Gentile P, Chiono V, Carmagnola I, Hatton PV. An overview of poly(lactic-coglycolic) acid (PLGA)-based biomaterials for bone tissue engineering. Int. J. Mol. Sci. 2014; 15:3640–3659. [PubMed: 24590126]
32. Shaw F-Z. Is spontaneous high-voltage rhythmic spike discharge in Long Evans rats an absence-like seizure activity? Journal of neurophysiology. 2004; 91:63–77. [PubMed: 12826656]
33. Pearce PS, et al. Spike–wave discharges in adult Sprague–Dawley rats and their implications for animal models of temporal lobe epilepsy. Epilepsy & Behavior. 2014; 32:121–131. [PubMed: 24534480]
34. Rodgers KM, Dudek FE, Barth DS. Progressive, seizure-like, spike-wave discharges are common in both injured and uninjured sprague-dawley rats: implications for the fluid percussion injury model of post-traumatic epilepsy. The Journal of Neuroscience. 2015; 35:9194–9204. [PubMed: 26085641]
35. Polikov VS, Tresco PA, Reichert WM. Response of brain tissue to chronically implanted neural electrodes. Journal of neuroscience methods. 2005; 148:1–18. [PubMed: 16198003]
36. Ryu SI, Shenoy KV. Human cortical prostheses: lost in translation? Neurosurgical focus. 2009; 27:E5. [PubMed: 19569893]
37. Biran R, Martin DC, Tresco PA. Neuronal cell loss accompanies the brain tissue response to chronically implanted silicon microelectrode arrays. Experimental neurology. 2005; 195:115–126. [PubMed: 16045910]
38. Biran R, Martin DC, Tresco PA. The brain tissue response to implanted silicon microelectrode arrays is increased when the device is tethered to the skull. Journal Biomedical Materials Research Part A. 2007; 82:169–178.
39. Hwang S-W, et al. A physically transient form of silicon electronics. Science. 2012; 337:1640–1644. [PubMed: 23019646]
40. Yin L, et al. Dissolvable metals for transient electronics. Adv. Func. Mater. 2014; 24:645–658.
41. Badawy WA, Al-Kharafi FM. Corrosion and passivation behaviors of molybdenum in aqueous solutions of different pH. Electrochimica Acta. 1998; 44:693–702.
42. Kang S-K, et al. Biodegradable thin metal foils and spin-on glass materials for transient electronics. Adv. Funct. Mater. 2015; 7:9297–9305.
43. Kang S-K, et al. Dissolution behaviors and applications of silicon oxides and nitrides in transient electronics. Adv. Func. Mater. 2014; 24:4427–4434.
44. Hwang S-W, et al. Dissolution chemistry and biocompatibility of single-crystalline silicon nanomembranes and associated materials for transient electronics. ACS Nano. 2014; 8:5843–5851. [PubMed: 24684516]
45. Kue R, et al. Enhanced proliferation and osteocalcin production by human osteoblast-like MG63 cells on silicon nitride ceramic discs. Biomaterials. 1999; 20:1195–1201. [PubMed: 10395388]
46. Bal BS, Rahaman MN. Orthopedic applications of silicon nitride ceramics. Acta Biomater. 2012; 8:2889–2898. [PubMed: 22542731]

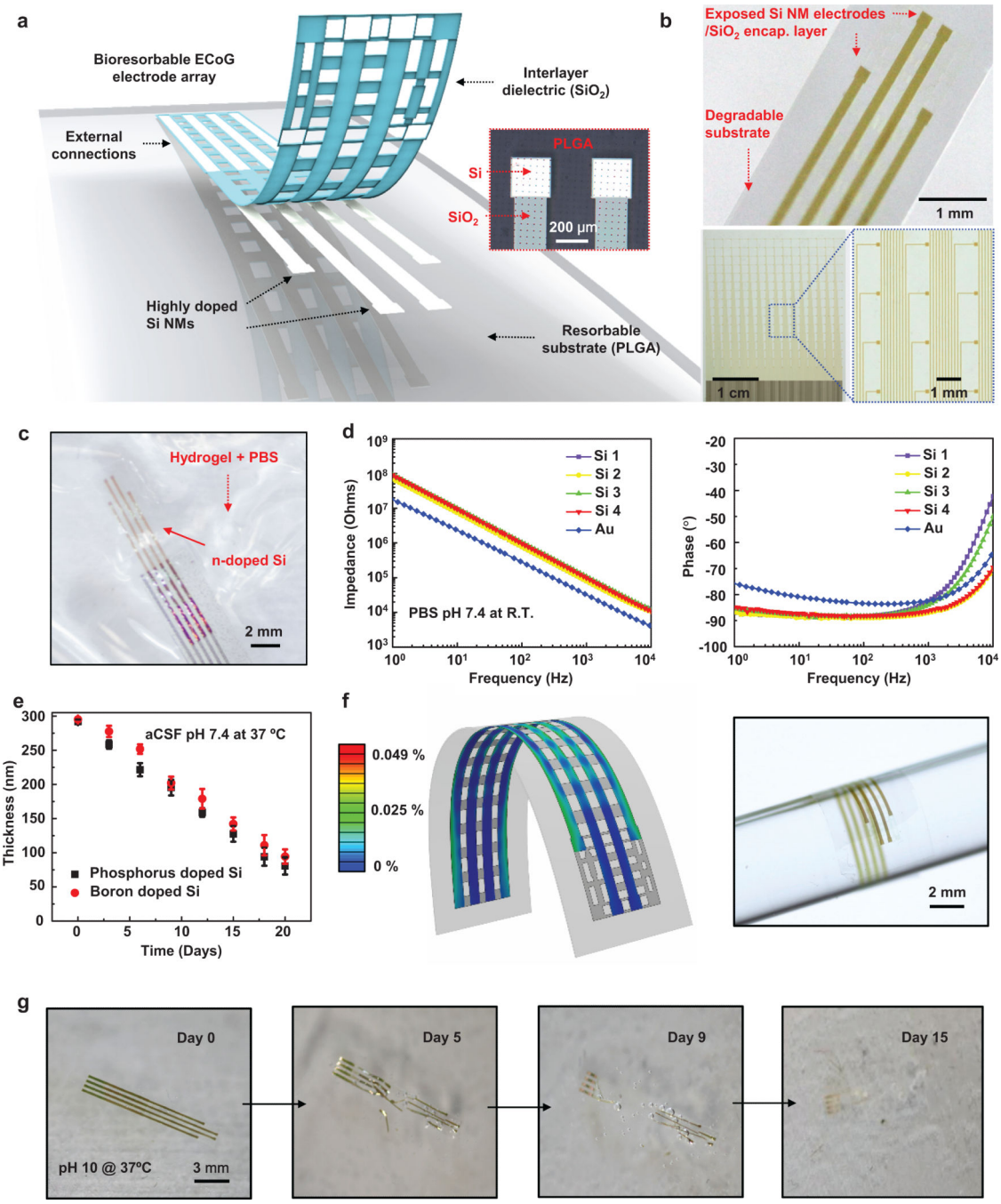

Figure 1. Thin, flexible neural electrode arrays with fully bioresorbable construction based on patterned silicon nanomembranes (Si NMs) as the conducting component

a, Schematic exploded view illustration of the construction of a passive, bioresorbable neural electrode arrays for ECoG and sub-dermal EEG measurements. A photolithographically patterned, n-doped Si NMs (~300 nm thick) defines the electrodes and interconnects. A film of SiO_2 (~100 nm thick) and a foil of PLGA (~30 μm thick) serves as a bioresorbable encapsulating layer and substrate, respectively. The device connects to an external data acquisition (DAQ) system through an anisotropic conductive film interfaced to the Si NMs interconnects at contact pads at the edge. A magnified optical image of electrodes on the

right highlights the sensing (Si NMs) and insulating (SiO_2) regions. **b**, Photographs of bioresorbable neural electrode arrays with 4 channels (top) and 256 (16 × 16 configuration) channels (bottom). **c**, Microscope image of a device on a hydrogel substrate immersed in an aqueous buffer solution (pH 7.4) at 37 °C. **d**, Electrochemical impedance spectra measured at four different recording sites in an array configured for ECoG. **e**, Dissolution kinetics for phosphorus and boron doped Si NMs (~300 nm thick, dopant concentration 10^{20} /cm^3) during immersion in artificial cerebrospinal fluid (aCSF) pH 7.4 at 37 °C. **f**, Distribution of principal strains extracted from finite-element modeling (FEM) of a device bent to a radius of curvature of 1 mm (center) and corresponding displacement profile (left) and image of an array wrapped around a cylindrical tube with a radius of 2 mm (right). **g**, Images collected at several stages of accelerated dissolution induced by immersion in an aqueous buffer solution (pH 10) at 37 °C.

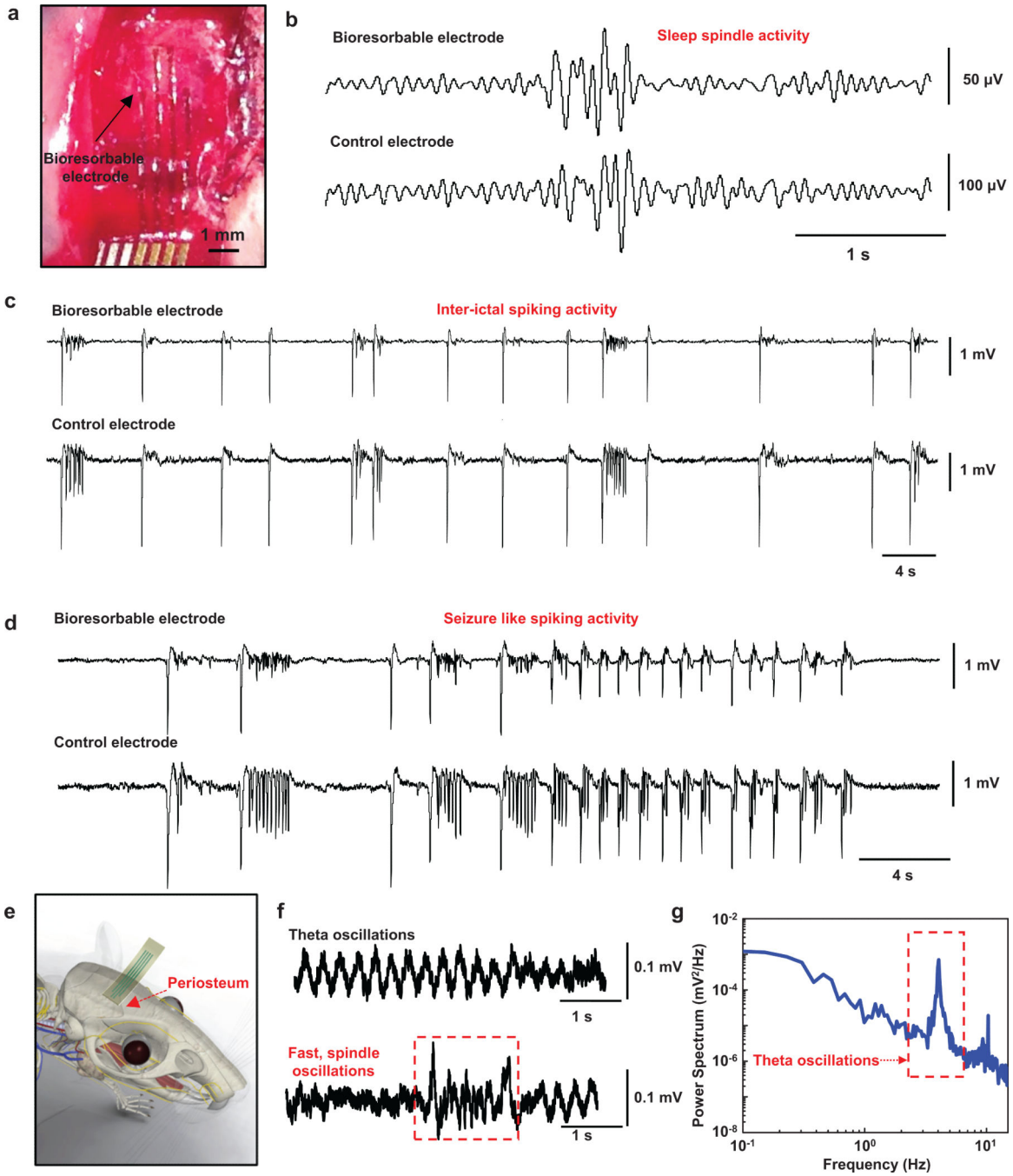

Figure 2. ***In vivo*** **neural recordings in rats using a passive, bioresorbable electrode array**

The data presented here are representative of three separate acute experiments, each with a duration of ~5-6 hours. **a,** Photograph of four-channel bioresorbable electrode array placed on the cortical surface of the left hemisphere of a rat. **b,** Sleep spindles recoded by a bioresorbable electrode and a nearby commercial stainless steel microwire electrode, as a control placed at 0.5 mm depth from the cortical surface. **c,** Interictal spiking activity captured by the bioresorbable electrode and the control electrode after topical application of bicuculine methodide. Both electrodes interface with the same hemisphere. Data were

processed through a 0.1 Hz-5 kHz bandpass filter. Recordings by the bioresorbable electrode and the control electrode show consistent interictal spikes. **d,** Interictal spiking activity recorded by the bioresorbable electrode and the control electrode 30 minutes after topical application of bicuculine methodide. Both recordings exhibit high signal-to-noise ratio (Si: 42, Control electrodes: 32) for detecting epileptiform activity. **e,** Cartoon illustration of a bioresorbable array placed on the periosteum for subdermal EEG recordings. **f,** Theta oscillations and fast spindle-like oscillations recorded subdermally using bioresorbable electrodes during isoflurane anesthesia. **g,** Power density spectra of the theta oscillations recorded over a 5 min time window. The spectrum shows a clear peak at the expected frequency range.

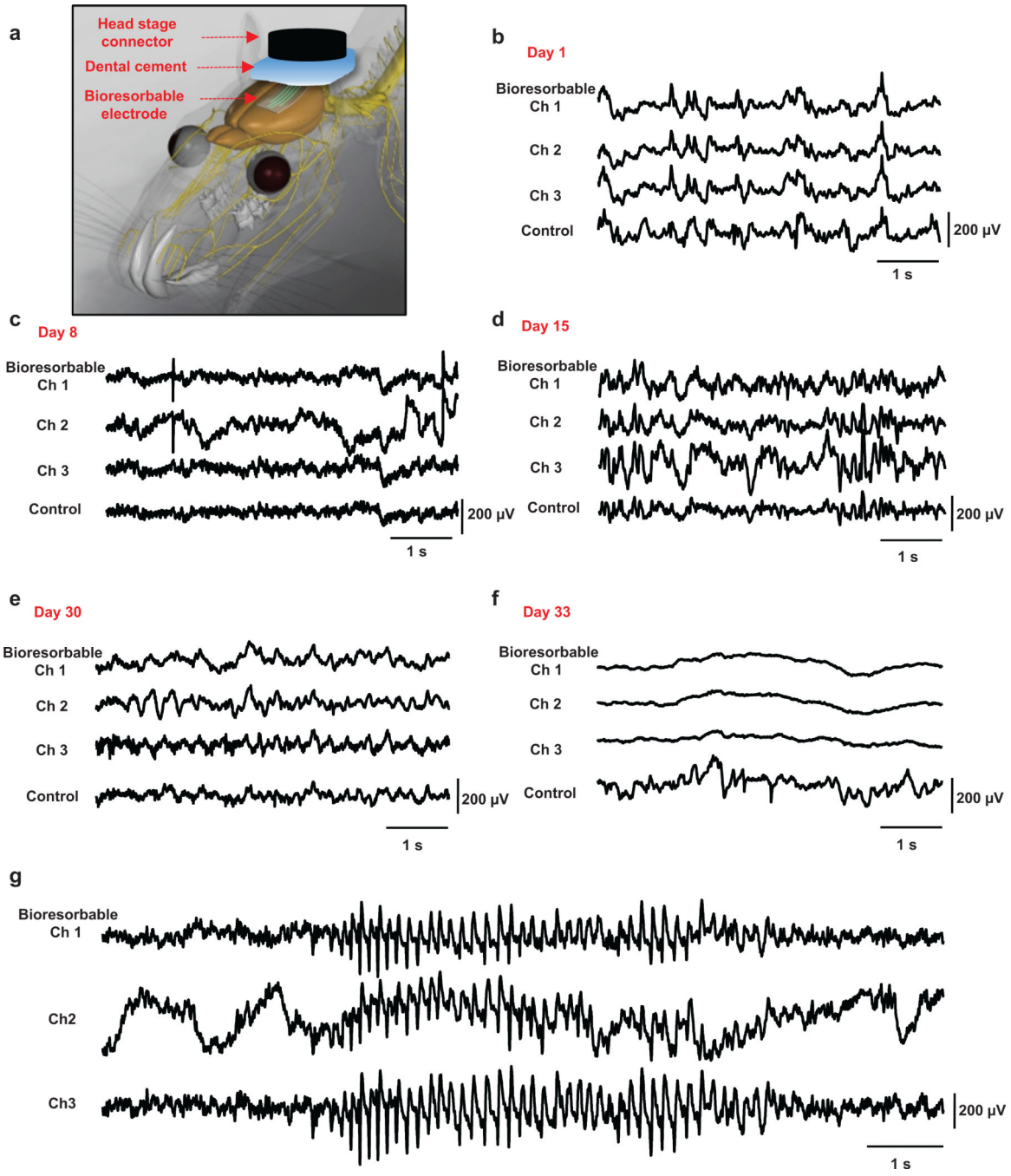

Figure 3. ***In vivo*** **chronic recordings in rats using a passive, bioresorbable electrode array**

The data presented here is representative of chronic recording experiments with a duration of 30 days. **a,** Photograph of a four-channel bioresorbable electrode array implanted on left hemisphere of the brain of a rat, for chronic recordings, with a coating gelfoam and a layer of dental cement. The array connects to a custom-built circular interface board through a flexible ACF cable. The inset shows the array and craniaotomy after application of a first layer of dental cement. **b-f,** Representative ECoG signals recorded by the bioresorbable array and the control electrode on day 1, 8, 15, 30 and 33. Recordings from three electrodes

from the bioresorbable array exhibit large scale oscillatory behavior consistent with small local and temporal variations. After functional dissolution (Day 33), signals from the bioresorbable array show no ECoG activity while the control electrode continues to show expected cortical potentials. **g,** High voltage rhythmic spikes observed during absence-like seizure activity recorded chronically.

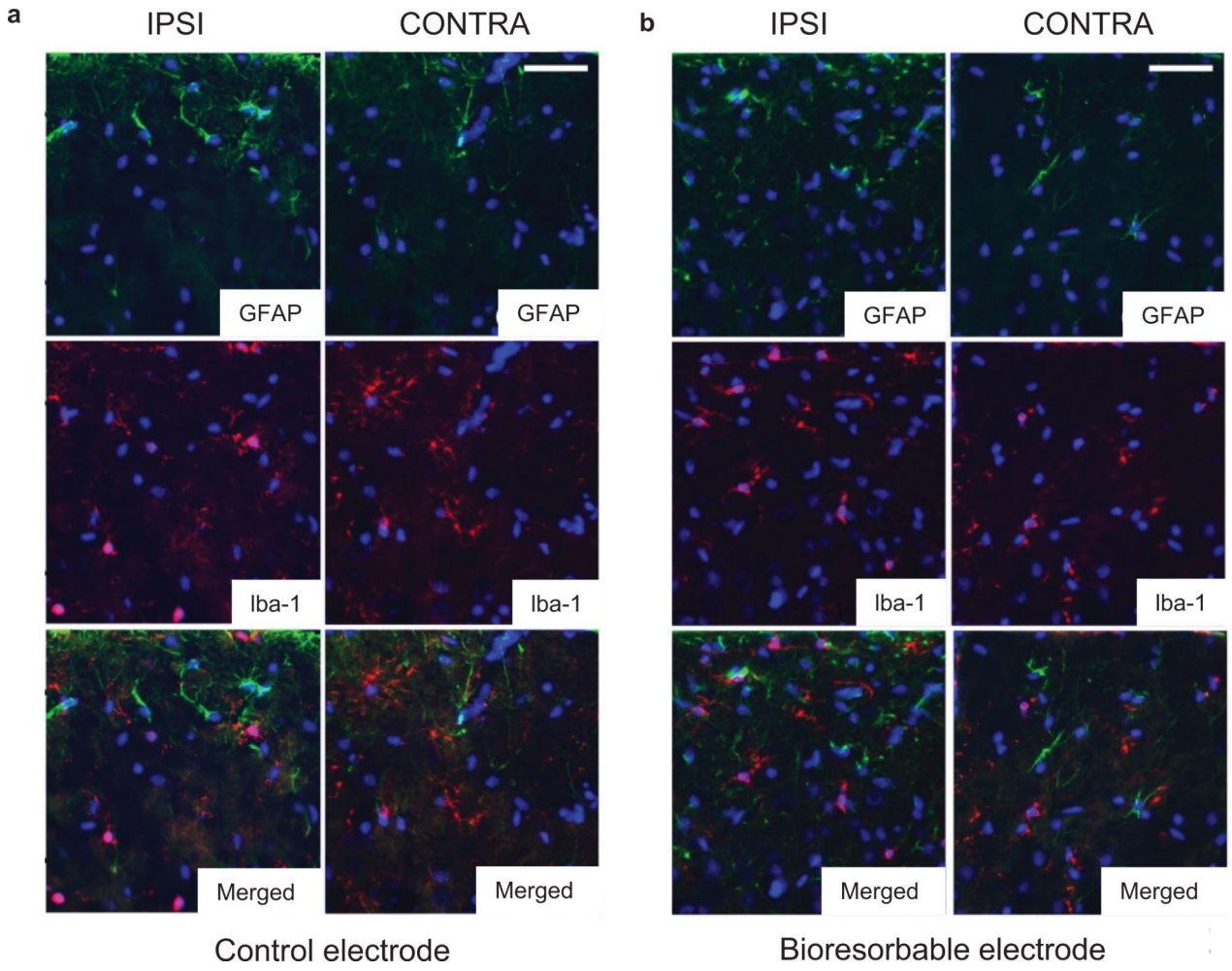

Figure 4. Immunohistology analysis

Double labeling for astrocytic marker GFAP (green) and microglia/macrophages marker Iba-1 (red) demonstrates moderate subpial gliosis at the implantation sites of both control (**a**, upper left panels) and bioresorbable (**b**, upper right panels) electrodes and a marked increase in the densities of activated round microglial cells, exclusively underneath the control electrodes (middle left panels). Cell nuclei are visualized with DAPI stain (blue). Scale bars represent 30 μm.

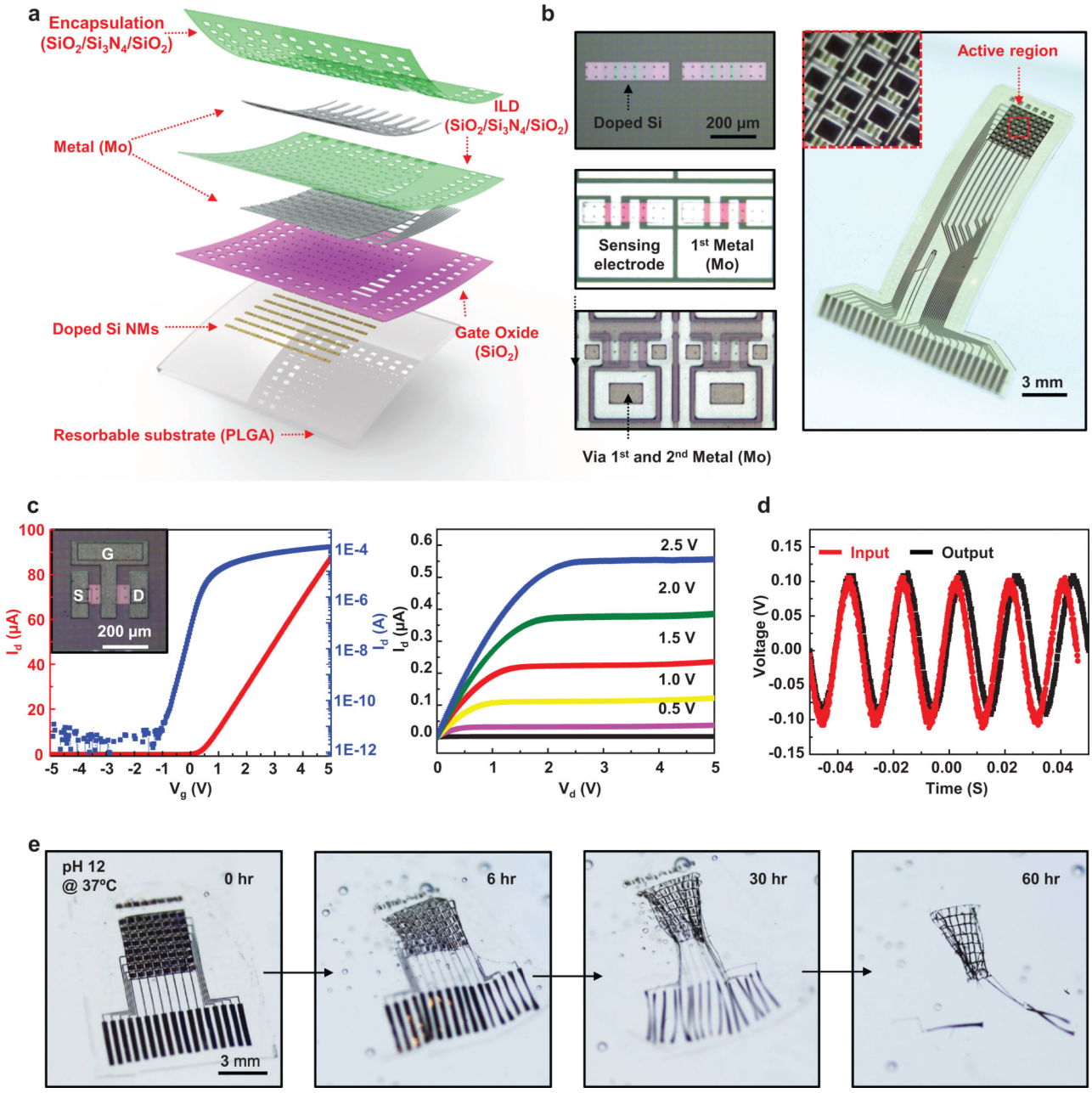

Figure 5. Bioresorbable actively multiplexed neural electrode array

a, Schematic exploded view illustration of an actively multiplexed sensing system for high resolution ECoG, in a fully bioresorbable construction. This 8 × 8 embodiment includes 128 metal-oxide-semiconductor field-effect transistors (MOSFETs) where Si NMs serve as both the active semiconductor material and the neural interface electrodes. The metallization, the gate dielectric and the interlayer dielectric rely on thin films of Mo (~300 nm thick) and SiO_2 (~100 nm thick) and trilayers of SiO_2 (~300 nm thick) / Si_3N_4 (~400 nm thick) /SiO_2 (~300 nm thick), respectively. A second layer of Mo (~300 nm thick) defines column interface lines. A similar trilayer serves as the encapsulation. A film of poly(lactide-co-glycolide) (PLGA, ~30 μm thick) forms the substrate. **b**, Optical micrograph images of a

pair of unit cells at various stages of fabrication (left) and a picture of a complete system (right). **c**, The left frame shows linear (red) and log scale (blue) transfer curves for a representative n-channel MOSFET, for V_g swept from −5 to +5 V. The channel length (L_{ch}), and width (W) are 15 μm and 80 μm, respectively. The threshold voltage, mobility and on/off ratio are ~1 V, ~400 $cm^2/V{\cdot}s$ and ~10^8, respectively, with Mo for source, drain and gate electrodes, and SiO_2 for gate dielectrics. The right frame shows current-voltage characteristics, for V_g from 0 to 2.5 V with 0.5 V steps. **d**, Output response of a unit cell with respect to an input sine wave (200 mV peak to peak) upon insertion in aqueous phosphate buffer solution (PBS, pH 7.4) at room temperature. **e**, Images collected at several stages of accelerated dissolution of a system immersed into an aqueous buffer solution (pH 12) at 37 °C.

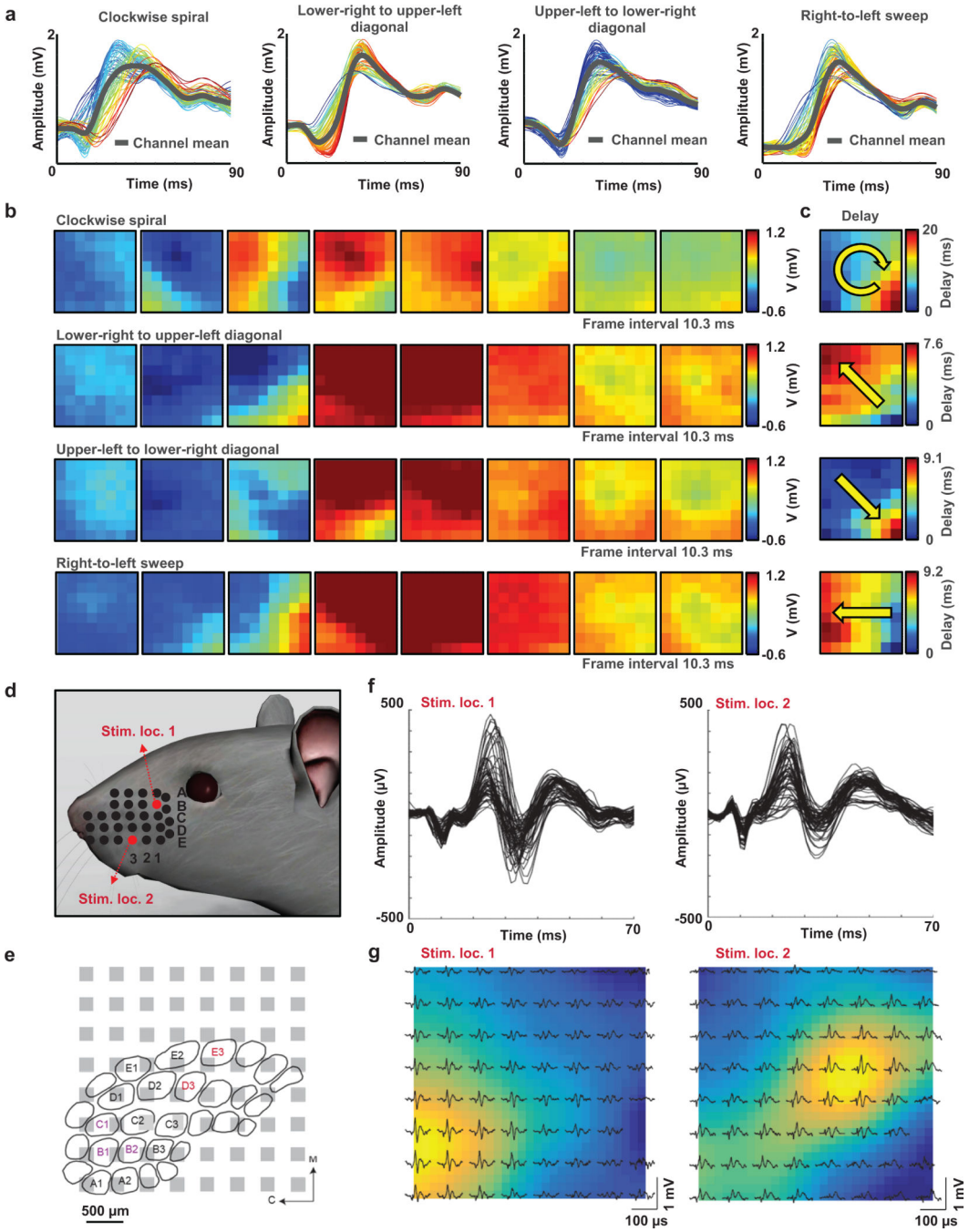

Figure 6. Acute *in vivo* microscale electrocortigoraphy (µECoG) with a 64-channel, bioresorbable, actively multiplexed array of measurement electrodes

a, Data recorded from picrotoxin-induced spikes (clockwise spiral, lower-right to upper-left diagonal, upper-left to lower-right diagonal, and right-to-left sweep). The results correspond to measurements across the 64 channels of the array, and the average response (grey) from all channels. The waveforms are color-coded according to the relative latency of the spike maximum (blue is earliest, red is latest). **b**, Movie frames corresponding to each spike pattern, showing the varied spatial-temporal µECoG voltage patterns from all 64 electrodes at the labeled time. Blue indicates negative, and dark red indicates the highest peak-to-peak

voltage observed for each electrode site. The frame interval and color scale are provided for each set of eight movie frames. **c**, Relative delay map for the band-pass filtered data of each spike activity from frame b, illustrating a clear phase singularity indicated by arrow. **d**, Illustration of the whisker stimulation locations (Stim. loc.: B1 and Stim. loc.: E3) in a rat model. **e**, Illustration of the barrel cortex and estimated relative location of the recording array based on evoked potential results. Visibly-activated whiskers indicated by color corresponding to the stimulation location. M = medial, C = caudal. **f**, Temporal characteristics of the potentials evoked by stimulation location 1 (left) and 2 (right). **g**,Spatial distribution of the potentials evoked by stimulation location 1 and 2. The color map indicates the evoked potential size, interpolated across the array.